Testing space-scale methodologies for automatic geomorphic feature extraction from lidar in a complex mountainous landscape

Paola Passalacqua,[1] Paolo Tarolli,[2,3] and Efi Foufoula-Georgiou[1]

Received 22 October 2009; revised 12 June 2010; accepted 22 June 2010; published 20 November 2010.

[1] The next generation of digital elevation data (≤3 m resolution) calls for the development of new algorithms for the objective extraction of geomorphic features, such as channel networks, channel heads, bank geometry, landslide scars, and service roads. In this work, we test the performance of two newly developed algorithms for the extraction of geomorphic features: the wavelet-based extraction methodology developed by Lashermes et al. (2007) and the GeoNet nonlinear diffusion and geodesic paths methodology proposed by Passalacqua et al. (2010). The study area is part of the Rio Cordon basin, a headwater alpine catchment located in the Dolomites, a mountainous region in the eastern Italian Alps. The aim of this work is to compare the capability of the two new algorithms in extracting the channel network and capturing channel heads, relevant channel disruptions corresponding to landslides, and representative channel cross sections. The extracted channel networks are also compared to the ones obtained using classical methodologies on the basis of an area threshold and an area-slope threshold. A high-resolution digital terrain model of 1 m served as the basis for such analysis. The results suggest that, although the wavelet-based methodology performs well in the channel network extraction and is able to detect channel heads and channel disruptions, the local nonlinear filter together with the global geodesic optimization used in GeoNet is more robust and computationally efficient while achieving better localization and extraction of features, especially in areas where gentle slopes prevail. We conclude that these new methodologies should be considered as valid alternatives to classical methodologies for channel network extraction from lidar, in addition to offering the potential for calibration-free channel source identification and also extraction of additional features of interest.

Citation: Passalacqua, P., P. Tarolli, and E. Foufoula-Georgiou (2010), Testing space-scale methodologies for automatic geomorphic feature extraction from lidar in a complex mountainous landscape, *Water Resour. Res.*, *46*, W11535, doi:10.1029/2009WR008812.

1. Introduction

[2] In the last decade, a range of new remote sensing techniques, such as terrestrial and airborne laser scanners, has led to a dramatic increase in terrain information [*Tarolli et al.*, 2009]. The terrestrial laser scanner provides very high resolution surveys over limited areas. The airborne laser scanner technology, also known as light detection and ranging (lidar), offers the opportunity to provide high-resolution topographic data over areas larger than other technologies [*Ackerman*, 1999; *Kraus and Pfeifer*, 2001; *Briese*, 2004; *Slatton et al.*, 2007]. A new generation of high-resolution (1–3 m) lidar-derived digital terrain models (DTMs) are now available for different landscapes, and widely used by several researchers, offering new opportunities for the scientific community. In the last few years several studies have been conducted using lidar data. These include: the characterization and differentiation of landslide morphology, such as the determination of the locations and distribution of landslide activity [*McKean and Roering*, 2004; *Glenn et al.*, 2006; *Ardizzone et al.*, 2007; C. Gangodagamage et al., Statistical signature of deep-seated landslides, submitted to *Journal of Geophysical Research*, 2009], the geomorphological mapping of glacial landforms [*Smith et al.*, 2006], the recognition of depositional features of alluvial fans [*Staley et al.*, 2006; *Frankel and Dolan*, 2007; *Cavalli and Marchi*, 2007] and of channel bed morphology [*Cavalli et al.*, 2008; *Trevisani et al.*, 2010], the calculation of slope for headwater channel network analysis [*Vianello et al.*, 2009], the analysis of the hillslope-to-valley transition morphology and of the topographic signature of valley incision by debris flows and landslides [*Tarolli and Dalla Fontana*, 2009], and some critical issues of high-resolution DTMs for the numerical modeling of shallow landslides [*Tarolli and Tarboton*, 2006]. The works of *Lashermes et al.* [2007], *Tarolli and Dalla Fontana* [2009], *Passalacqua et al.* [2010], and *Pirotti and Tarolli*

[1]National Center for Earth-Surface Dynamics and St. Anthony Falls Laboratory, Department of Civil Engineering, University of Minnesota-Twin Cities, Minneapolis, Minnesota, USA.
[2]Department of Land and Agroforest Environments, University of Padova, Padua, Italy.
[3]Institute of Inland Waters, Hellenic Center for Marine Research, Anavyssos, Greece.

0043-1397/10/2009WR008812

[2010] discussed a topic that has been the subject of considerable research over the past several decades: the automatic extraction of channel networks from high-resolution lidar-derived DTMs. Different methods have been proposed in the literature for channel network extraction. For example, a constant critical support area [e.g., *O'Callaghan and Mark*, 1984; *Band*, 1986; *Mark*, 1988; *Tarboton et al.*, 1989, 1991], a slope-dependent critical support area [e.g., *Montgomery and Dietrich*, 1992; *Dietrich et al.*, 1993], and also a threshold on local curvature [*Rodriguez-Iturbe and Rinaldo*, 1997; *Heine et al.*, 2004]. The availability of high-resolution topography given by laser scanners offers now the opportunity to reconsider the procedures for channel network extraction introducing new methodologies and reaching more detailed results than those obtained in the past. It has to be kept in mind, however, that the resolution of the available DTMs and also the vertical error in the elevation data can considerably influence the accuracy, and thus interpretation, of the numerically computed local gradients and curvatures, both critical properties for channel extraction.

[3] In the work of *Lashermes et al.* [2007] a methodology based on wavelets was introduced to locally filter lidar elevation data, and to detect thresholds in topographic curvature and slope direction change for defining valleys and probable channelized portions of the valleys. This research indicated the effectiveness of high-resolution elevation data and of the related topographic curvature maps in the analysis of land surface morphology. The curvature derived from high-resolution topography using airborne lidar seems to greatly improve channel network extraction since it is possible to recognize in detail concave-convergent terrain associated with fluvial erosion processes [*Tarolli and Dalla Fontana*, 2009]. Furthermore the work of *Passalacqua et al.* [2010] shows the advantages obtained using nonlinear filtering, instead of linear filtering as in the wavelet-based methodology, and the efficiency of geodesics in tracing channels. Nonlinear filtering is in fact capable of achieving 'noise' reduction (meaning observational noise or irregularities at scales smaller than the scales of interest), while enhancing geomorphic features of interest, without deforming landscape contours. In addition, the definition of channels as geodesics, that is, lines along which a certain cost function is minimized, allows a fully automatic and fast network extraction.

[4] The aim of this paper it to test and compare the relative merits of the methodologies proposed by *Lashermes et al.* [2007] and *Passalacqua et al.* [2010] in terms of their capability of extracting geomorphic features of interest such as channels, channel heads, detecting relevant channel disruptions corresponding to landslides, and capturing representative channel cross sections. The study area is part of the Rio Cordon basin, a headwater alpine catchment located in the Dolomites, a mountainous region in the eastern Italian Alps. We selected this area because several field surveys were conducted during the past few years, including lidar, field mapped channels, channel heads and landslide scars. These precious data sets give us the opportunity to discuss new issues, and test new analysis procedures when mapping channel networks in an alpine environment with a complex morphology. In particular, after presenting the study area (section 2) and reviewing briefly the two methodologies (section 3), we extract the channel networks and compare them to the ones obtained through classical methodologies (area and area-slope thresholds) (section 4). Then, we take advantage of the survey data available, to focus on the ability of the new methodologies to localize channel heads (section 5). As pointed out by *Lashermes et al.* [2007] and *Passalacqua et al.* [2010] and recalled later in this paper, the methodologies produce 'skeletons' of likely channelized pixels which are discontinuous, meaning that the probable channels exhibit disruptions, which may or may not represent geomorphologic features of interest. We investigate the nature of these disruptions by taking advantage of the availability of survey-mapped landslides in section 6. Furthermore, the effect of linear versus nonlinear filtering is analyzed through the investigation of cross sections extracted along the channels of the study area (section 7). Finally, we suggest a guideline for such applications, and also identify future challenges in fully or almost fully automated methodologies for geomorphic feature extraction from lidar (section 8).

2. Study Area

[5] The study area (Figure 1) consists in the Rio Col Duro basin (subbasin of Rio Cordon), a small headwater basin of 0.45 km^2, and some neighboring landslide areas, located in the Dolomites, a mountainous region in the eastern Italian Alps. The elevation ranges from 1935 to 2385 m a.s.l. with an average of 2199 m. The slope angle is 25.9° on the average and 74° at maximum, computed from the high-resolution DTM (1 m resolution) of the area in analysis. The basin is morphologically divided into two parts: the upper part consists of a low-slope belt dominated by colluvial channels; the lower part displays steep slopes and a narrow valley, where bedrock and alluvial channels and shallow landslides are present.

[6] The area has a typical alpine climate with a mean annual rainfall of about 1100 mm. Precipitation occurs mainly as snowfall from November to April. Runoff is dominated by snowmelt in May and June, but summer and early autumn floods represent an important contribution to the flow regime. During summer, storm events are usually separated by long dry spells. Soil thickness varies between 0.2 and 0.5 m on topographic spurs to depths of up to 1.5 m on topographic hollows. The vegetation covers 97% of the basin and consists of high-altitude grassland (91% of the area), and sporadic tall forest (6%). The remaining 3% of the area consists of bedrock outcrops and unvegetated talus deposits. Several field surveys were conducted during the past few years including lidar surveys (data acquired during snow-free conditions in October 2006) [*Pirotti and Tarolli*, 2010]. A recent campaign (September–October 2008, and August 2009) has provided new detailed data of field-mapped alluvial and colluvial channels, channel heads, and landslide scars in a neighboring area [*Pirotti and Tarolli*, 2010].

[7] The shallow landslides in the study area were documented by repeated surveys in the period 1995–2001 [*Dalla Fontana and Marchi*, 2003], and summer 2008–2009 based on Differential Global Positioning System (DGPS) ground observations. Analysis of these data indicates that small, shallow debris flow scars heal rapidly, and are difficult to detect after as few as 3–4 years. About 68% of the surveyed landslides were triggered by a very intense and short-duration storm on 14 September 1994 [*Lenzi*, 2001; *Lenzi et al.*,

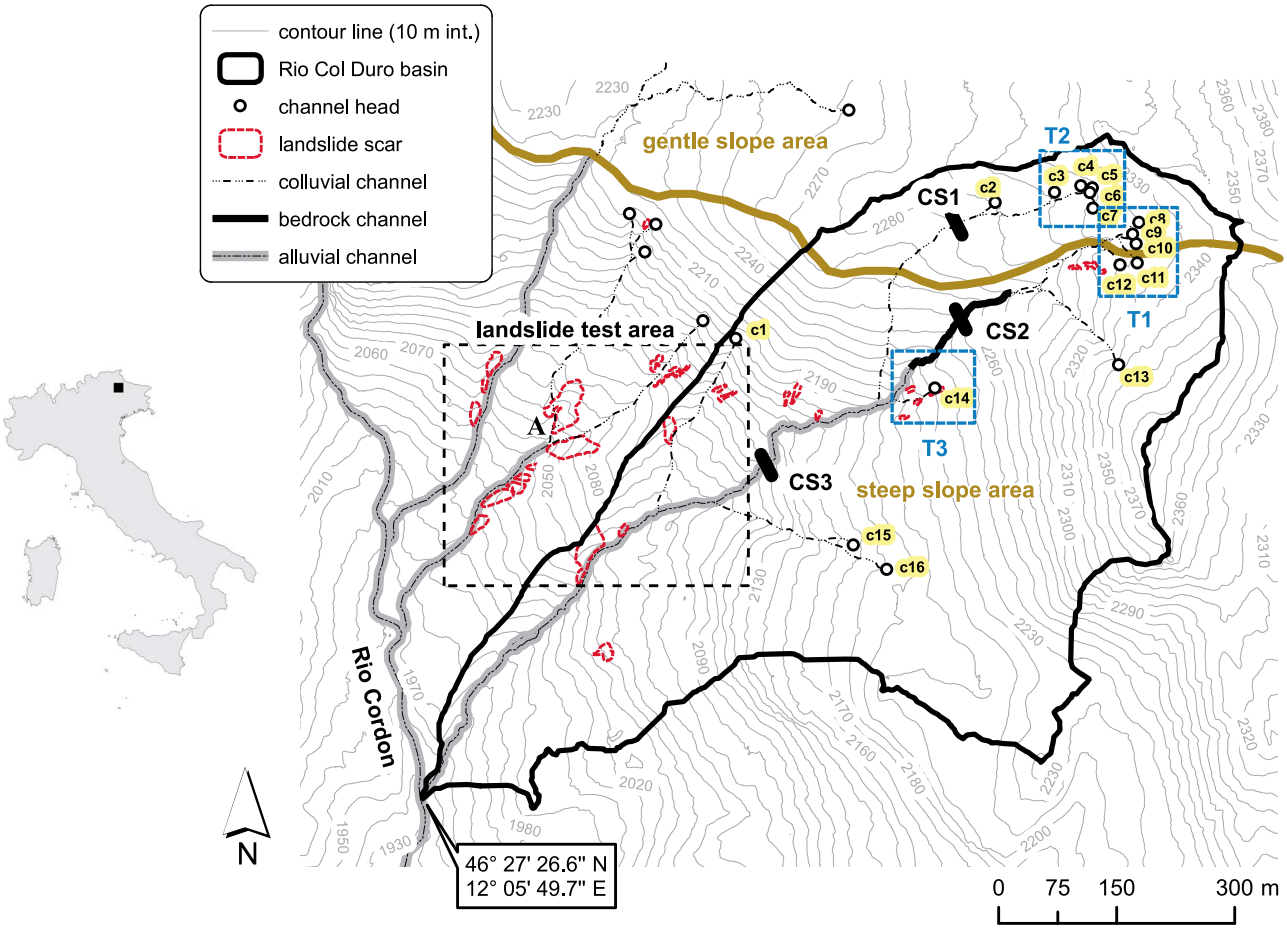

Figure 1. The Rio Col Duro basin. Shown is a location map of the study area, the channel head locations *c*, the areas where the analysis of channel heads detection is performed (T1, T2, and T3), and the area where landslide disruptions are analyzed landslide test area). The locations of three extracted cross sections are also marked (CS1, CS2, and CS3). The letter A indicates the largest landslide considered in this study. Landslide A is located at 46°27′39.921″N, 12°6′0.103″E, while the outlet has latitude 46°27′26.6″N and longitude 12°05′49.7″E.

2004]. The storm, with a duration of 6 h, caused the largest flood recorded in 20 years of observation in the Rio Cordon basin. Due to the short duration of the storm, few slope instabilities were observed on entirely soil-covered slopes, while several landslides were triggered on slopes just below rocky outcrops [*Tarolli et al.*, 2008]. An important new sediment source was formed on 11 May 2001, during an intense snowmelt event without rainfall following a very snowy winter [*Lenzi et al.*, 2003, 2004]. Soil saturation mobilized a shallow landslide (see landslide *A* in Figure 1) covering an area of 1905 m^2 which then turned into a mudflow moving along a small tributary. A 4176 m^3 debris fan was formed at the confluence with the Rio Cordon, providing to the main channel fine sediments to be transported downstream [*Lenzi et al.*, 2003]. This new landslide area triggered during 2001 is considered in this work, and it is located in a neighboring area of the Rio Col Duro basin where steep slopes, a narrow valley, and ancient landslide deposits are present. The location map of Rio Col Duro and the available surveyed data (channels, channel heads and landslides) are shown in Figure 1.

[8] It is important to note that the Rio Col Duro basin exhibits a significant variability in the values of drainage area at the channel heads. Namely, among the 16 channel heads included in the basin, the channel initiation drainage area ranges between 110 m^2 and 13000 m^2 approximately, as it can be seen from the histogram of drainage areas in Figure 2, computed using the D8 algorithm [*O'Callaghan and Mark*, 1984]. It is clear that it would be impossible to capture such a variability with a unique threshold value for drainage area, as it would be required by a classical extraction methodology. The small values of contributing area at several channel heads (channel 2 up to channel 10, see Figure 1) are explained by the formation of these tributaries not by a combination of flow accumulation and slope, but by subsurface flow in low-slope areas. Figure 3 and Figure 4 show examples of these two types of channel initiation processes observed in the Rio Cordon basin. In particular, Figure 3 shows an example of channel head generated by erosion, while Figure 4 shows a channel head generated by subsurface flow and gentle slope.

2.1. Field Data Collection

[9] Field surveys were carried out along the entire hydrographic network. The catchment was systematically

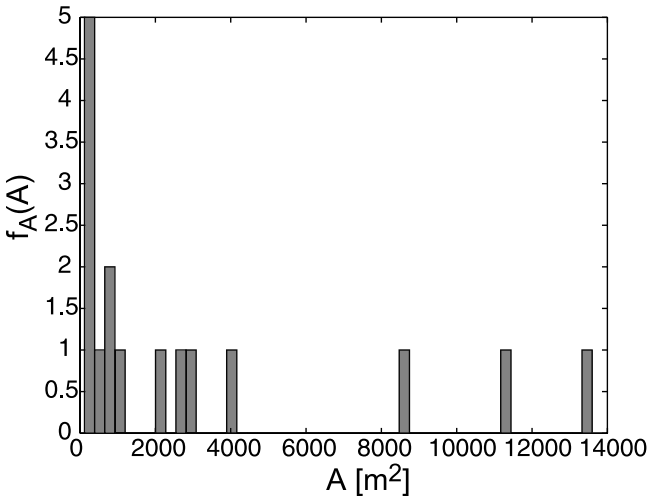

Figure 2. Histogram of the drainage area at the surveyed channel heads (a total of 16 channel heads) in the Rio Col Duro basin, computed using the D8 algorithm. The values of drainage area show a large variability, as they range between approximately 110 m^2 and 13000 m^2.

walked along all the drainage lines up to the catchment divide. The channel head, or first-order stream head, was defined as the point at which nonconfined divergent flows on the hillslope converged to a drainage line, i.e., the upstream limit of concentrated flow [*Dietrich and Dunne*, 1993].

Figure 3. An example of channel head observed in the Rio Col Duro basin formed by a combination of flow accumulation and slope (c13 in Figure 1).

Figure 4. An example of channel head observed in the proximity of the Rio Col Duro basin and formed by subsurface flow in a low-slope area. The flow accumulation at channel heads of this type of channels can be of the order of just 100 m^2.

[10] The channel network identified in the Rio Col Duro basin can be divided into three portions: colluvial, bedrock, and alluvial channels (see Figure 1). The colluvial incisions are small headwater channels, exhibiting a weak or ephemeral transport capacity [*Montgomery and Buffington*, 1997]. They can be considered as the elementary component of the hydrologic network, defining channel initiation [*Montgomery and Dietrich*, 1989], and characterizing the headwater areas. In our study area these morphologies are dominant in the upper part of the basin, where gentle slope prevails. The initiation process is due to an upslope infiltration of water within moraine deposits, and downslope subsurface flow where gentle slope soil mantle prevails. Nevertheless, colluvial channels are also present in the lower and steeper part of the basin, where their formation is mainly due to flow accumulation and surface erosion due to larger values of slope. The alluvial channel network (lower midzone of the network) is dominated by erosional and depositional processes controlled mainly by local slope changes, where the sediment forming the channel bed can be transported and organized during floods. Alluvial channels are characterized by bed morphologies such as cascades and steep pools, typical of steep mountainous channel reaches, characterized by high transport capacity [*Vianello and D'Agostino*, 2007].

2.2. Lidar Data Specifications

[11] The lidar data and high-resolution aerial photographs were acquired from an helicopter using an ALTM 3100 OPTECH, and Rollei H20 digital camera flying at an average altitude of 1000 m above ground level during snow-free conditions in October 2006. The flying speed was 80 knots, the scan angle 20° and the pulse rate 71 kHz. The survey design point density was specified to be greater than 5 points/m^2, recording up to 4 returns, including first and last. Lidar point measurements were filtered into returns from vegetation and bare ground using the Terrascan^{TM} software classification routines and algorithms. The lidar bare ground data set was used to generate a Digital Terrain Model (DTM) of 1 m grid cell size. The absolute vertical accuracy, evaluated by a direct comparison between lidar and ground DGPS elevation points, was estimated to be less than 0.3 m, an acceptable value for many lidar analyses in the field of geomorphology [*McKean and Roering*, 2004; *Glenn et al.*, 2006; *Frankel and Dolan*, 2007; *Tarolli and Dalla Fontana*, 2009]. Note that *Pirotti and Tarolli* [2010] demonstrated for the same study area used here (and the same data set) the suitability of this DTM vertical accuracy (and thus of the lidar bare ground point density) for an acceptable channel network extraction through the use of landform curvature maps. Digital aerial photos at a resolution of 0.15 m were also collected using a Rollei H20 camera.

3. Overview of the Two-Channel Extraction Methodologies

[12] In this section we present the mathematical background on the wavelet-based river network extraction methodology proposed by *Lashermes et al.* [2007] and the more recent one proposed by *Passalacqua et al.* [2010], based on advanced image processing techniques. The approach proposed by *Lashermes et al.* [2007] consists of using wavelets for the computation of slope direction change and curvature, which, as explained in the following subsection, are important metrics in channel detection and extraction. The wavelet tool developed by *Lashermes et al.* [2007] naturally leads to a multiscale analysis of the geomorphic features. The work of *Passalacqua et al.* [2010] has suggested important changes to improve the localization of the extracted channels and the automation and computational robustness of the algorithm. A brief description of the two methodologies follows. We refer the reader to *Lashermes et al.* [2007] and *Passalacqua et al.* [2010] for more details on the extraction methodologies.

3.1. Wavelet-Based Framework for Feature Extraction

[13] Local slopes, $|\nabla h|$, and local curvatures, $\nabla^2 h$ (using here the Laplacian as definition of curvature), carry considerable information about the type of landscape form at a site (e.g., valley, channel, hillslope, hollow). In particular, if a site i has $\nabla^2 h_i < 0$, the site is topographically convex, or divergent, and is conventionally defined as a hillslope. If $\nabla^2 h_i \geq 0$, the site is topographically concave, or convergent, and typically corresponds to a valley (channelized or not), hollow or basal hillslope sculpted by advective processes.

[14] There are two different ways in which *scale* comes into the picture in the analysis of topographic data. First, there is the scale at which elevation data are available, usually called resolution. Second, there is a scale of averaging or smoothing that is often applied when computing local geomorphic properties. This smoothing is performed to reduce the effect of noise (observational noise or irregularities at scales smaller than the scale of interest) on the numerical estimation of local derivatives from discrete data. This smoothing can be done traditionally in two different ways. One is to perform a spatial averaging of the pointwise derivatives, and the other is to spatially average the topography field and then take derivatives of the smoothed field. As shown by *Lashermes et al.* [2007], smoothing the topography data with a Gaussian filter and then take first and second derivatives of the smoothed topography is mathematically equivalent to computing the wavelet coefficients of the topography using as wavelet filters the first and second derivatives of the Gaussian function, respectively. This is a direct consequence of the well-known commutative property of the convolution operation:

$$\partial_x (f \star g) = \partial_x f \star g = f \star \partial_x g \tag{1}$$

which implies that smoothing the function f with a kernel g and then taking derivatives (left most term) is equivalent to taking derivatives of the function and smoothing these derivatives with the kernel g (middle term) or equivalent to smoothing the function f directly with the derivative of the kernel g (right most term). This is an important property and its first two terms correspond to the smoothing methods just described. The third term of the above equality (1) naturally introduces the use of wavelets for efficient computation of local slopes and curvatures of a function. Specifically, the first and second derivatives of the function $h(x, y)$ in the x direction (similar expressions hold for the y direction) can be written as

$$\nabla_{x,\sigma} h(x,y) = (h \star g^x_{1,\sigma,x,y})(x,y) \tag{2}$$

$$\nabla^2_{x,\sigma} h(x,y) = (h \star g^x_{2,\sigma,x,y})(x,y) \tag{3}$$

where

$$g^x_{1,\sigma,x,y}(u,v) = \partial_x g_{0,\sigma,x,y} \tag{4}$$

$$g^x_{2,\sigma,x,y}(u,v) = \partial^2_x g_{0,\sigma,x,y} \tag{5}$$

where σ represents the standard deviation of the Gaussian kernel, the subscripts 1 and 2 indicate the order of the derivative, the superscript x indicates the direction in which the derivative is taken, and $g_{0,\sigma,x,y}$ is a 2D Gaussian kernel of standard deviation σ and centered at location (x, y):

$$g_{0,\sigma,x,y}(u,v) = \frac{1}{2\pi\sigma^2} \exp\left[-\frac{(u-x)^2 + (v-y)^2}{2\sigma^2}\right] \tag{6}$$

We note that the above kernels (4) and (5) are proper wavelets; that is, they satisfy the admissibility conditions of having local support and integral zero. By varying the variance σ of the Gaussian filter $g_{0,\sigma,x,y}$ (6) the above computations can be performed at different scales simultaneously.

[15] The scale a associated with a wavelet $\psi(a, x)$ is defined from its Fourier transform $\tilde{\psi}(a, \nu)$: this has necessarily a

well-defined maximum (a wavelet can be interpreted as a band-pass filter) at a specific frequency ν_m. The scale a is then defined as the inverse of this band-pass frequency: $a = \frac{1}{\nu_m}$ [e.g., *Mallat*, 1998; *Kumar and Foufoula-Georgiou*, 1997]. Based on this, the scale a associated with the wavelets $g^x_{1,\sigma,x,y}$ and $g^y_{1,\sigma,x,y}$ is related to the parameter σ through the relation

$$a = 2\pi\sigma \tag{7}$$

[16] The scale a associated with the wavelets $g^x_{2,\sigma,x,y}$ and $g^y_{2,\sigma,x,y}$ is related to the parameter σ through the relation

$$a = \sqrt{2}\pi\sigma \tag{8}$$

[17] Since the scale a of smoothing is a more relevant and easier to interpret quantity than the parameter σ of the analyzing wavelet, all the notations for slope and curvature computed using wavelets will be labeled with a and not σ in the sequel. Note that a single choice for the scale a corresponds to different σ values for the g_1 and g_2 wavelets and thus for gradients and curvatures. The expression for the modulus $m_a(x, y)$ of the steepest slope at location (x, y) and scale a is given by

$$m_a(x,y) = \sqrt{(\nabla_{x,a}h(x,y))^2 + (\nabla_{y,a}h(x,y))^2} \tag{9}$$

where again the subscript x and a indicate the direction and scale at which the derivative is taken, respectively. Channel incision in uplands topography leads to hillslopes on opposite sides that typically face each other obliquely. This signature can be used to delineate the axis of valleys and the likely pathway of channels with limited floodplain area on their boundaries [*Lashermes et al.*, 2007]. This can be achieved by computing the derivative of the slope direction $\theta_a(x, y)$ given by

$$d\theta_a = \sqrt{(d_x\theta_a)^2 + (d_y\theta_a)^2} \tag{10}$$

where

$$\begin{aligned}\theta_a(x,y) &= \arctan\left(\frac{\nabla_{y,a}h(x,y)}{\nabla_{x,a}h(x,y)}\right) \quad \text{if} \quad \nabla_{x,a}h(x,y) > 0 \\ &= \pi + \arctan\left(\frac{\nabla_{y,a}h(x,y)}{\nabla_{x,a}h(x,y)}\right) \quad \text{if} \quad \nabla_{x,a}h(x,y) < 0 \\ &\quad \text{and } \nabla_{y,a}h(x,y) > 0 \\ &= -\pi + \arctan\left(\frac{\nabla_{y,a}h(x,y)}{\nabla_{x,a}h(x,y)}\right) \quad \text{if} \quad \nabla_{x,a}h(x,y) < 0 \\ &\quad \text{and } \nabla_{y,a}h(x,y) < 0\end{aligned} \tag{11}$$

and finding the points at which $d\theta_a$ becomes maximum [see *Lashermes et al.*, 2007]. Finally, the Laplacian is given by

$$\gamma_a(x,y) = \nabla^2_{x,a}h(x,y) + \nabla^2_{y,a}h(x,y) \tag{12}$$

[18] In *Lashermes et al.* [2007] the above multiscale properties $\gamma_a(x, y)$ and $d\theta_a(x, y)$ were used to extract channel networks from lidar. Specifically, the analysis of the quantile-quantile plots of the Laplacian curvature and slope direction change across scales highlighted the existence of two transitions in the statistical behavior of these metrics [*Lashermes et al.*, 2007]. It was found that a sharp deviation in the positive tail of the probability distribution of curvature from a Gaussian distribution defined a critical threshold curvature which delineates the channelized valleys of the terrain, while the similarly identified threshold in the slope direction change indicates the transition between non-channelized and channelized parts of the valley. The two thresholds are used to create the set of the likely channelized pixels, namely a binary matrix called 'skeleton' where pixels that satisfy the threshold criteria are assigned a value of 1, while pixels that do not satisfy them are assigned a value of 0. The skeleton is then used as a starting point for the semiautomatic channel extraction. The same skeleton will also be used here for investigating the capabilities of this methodology to detect channel morphology properties.

[19] After the identification of the likely channelized pixels through the quantile-quantile plots of curvature and slope direction change, *Lashermes et al.* [2007] performed the extraction of the channels in a semiautomatic fashion. Starting from the skeleton, the user manually selects the outlet of the basin and the extraction proceeds upstream linking all the pixels that have maximum slope direction change along the main stem. Then the procedure is repeated for each tributary junction. The extraction algorithm stops when one or both of the threshold criteria on curvature and slope direction change are not satisfied, as at these locations the skeleton is interrupted. Note that this semiautomatic methodology requires in some cases manual intervention and the resulting extracted channel network is affected by the user choice on which channels to trace (if the skeleton appears very disrupted along a certain path, the user may decide that it is not a channel and avoid tracing it).

3.2. Geometric Nonlinear Framework for Feature Extraction

[20] The Gaussian filtering operation, performed in the *Lashermes et al.* [2007] methodology, can be expressed as

$$h(x,y;a) = h_0(x,y) \star G(x,y;\sigma) \tag{13}$$

where $h_0(x, y)$ represents the original high-resolution digital elevation data, $G(x, y; \sigma)$ is a Gaussian kernel of variance σ^2 and centered at location (x, y), and $h(x, y; a)$ represents the resulting family of coarsened landscapes at scales $a = 4\sigma$. The operation in (13) is equivalent to applying an isotropic diffusion equation over time, with the initial condition $h(x, y; 0) = h_0(x, y)$ and where time relates to scale a:

$$\partial_t h(x,y;t) = \nabla \cdot (c\nabla h) = c\nabla^2 h \tag{14}$$

where the subscript t indicates that the derivative is taken in time, c is the constant diffusion coefficient and ∇ is the gradient operator. Because of the isotropic nature of the Gaussian filtering operation, diffusion acts across the landscape, without respecting the natural boundaries of the features. This operation results in a degradation of the spatial localization of these boundaries, which, in the case of landscapes, represent important discontinuities such as crests and valleys. For this reason, the methodology proposed by *Passalacqua et al.* [2010], released to the community as

GeoNet, substitutes the Gaussian filter with a nonlinear filter, originally formulated by *Perona and Malik* [1990]. The nonlinear filter results in a spatially variable anisotropic diffusion, by making the diffusion coefficient c of the standard linear diffusion equation (14) a suitable function of space. The nonlinear diffusion equation is thus formulated as follows:

$$\partial_t h(x,y;t) = \nabla \cdot [c(x,y,t)\nabla h] = c(x,y,t)\nabla^2 h + \nabla c \cdot \nabla h \quad (15)$$

[21] It is desired that the diffusion coefficient c is chosen such that the nonlinear filter achieves noise reduction and edge enhancement, avoiding smoothing across boundaries. In principle, if the location of the boundaries were known, then we could set $c = 0$ at the boundary and $c = 1$ everywhere else. According to *Perona and Malik* [1990] the gradient of elevation gives a simple first estimate of the boundaries location:

$$\vec{E}(x,y;t) = \nabla h(x,y;t) \quad (16)$$

resulting in the diffusion coefficient c being a function of the magnitude of the gradient:

$$c = p(|\nabla h|) \quad (17)$$

[22] *Perona and Malik* [1990] suggested the following two forms of $p(\cdot)$, the so-called *edge-stopping function*, able to avoid diffusion across boundaries:

$$p(|\nabla h|) = \frac{1}{1 + (|\nabla h| / \lambda)^2} \quad (18)$$

or

$$p(|\nabla h|) = e^{-(|\nabla h|/\lambda)^2} \quad (19)$$

where λ is a constant that can be estimated from the 90% quantile of the probability distribution function of the absolute values of the gradient throughout the image [*Perona and Malik*, 1990]. The nonlinear diffusion equation takes the following form:

$$\partial_t h(x,y;t) = \nabla \cdot [p(|\nabla h|)\nabla h] \quad (20)$$

[23] This nonlinear filter is used to reduce the noise in the digital elevation data and enhance the features of interest. *Passalacqua et al.* [2010] showed the advantages of using the Perona-Malik filter (nonlinear diffusion) versus the Gaussian filter (linear diffusion) through the application to a basin located in northern California. The form of the edge-stopping function used is (18).

[24] Following the nonlinear filtering operation, we can proceed, as in the wavelet-based methodology, with creating a skeleton of the likely channelized pixels. *Passalacqua et al.* [2010] suggest to use the quantile-quantile plot of curvature (as in work by *Lashermes et al.* [2007]) and then to further narrow the skeleton by introducing a small threshold in the contributing area, small enough to not interfere with channel initiation, but large enough to effectively reduce the presence of isolated convergent areas which appear as noise in the skeleton (they are small isolated areas and thus do not necessarily belong to channels). Note that *Passalacqua et al.* [2010] employ the definition of geometric curvature $\kappa = \nabla \cdot (\nabla h/|\nabla h|)$ instead of the Laplacian. The geometric curvature, being the gradients normalized by their magnitude, attains an easier comparative interpretation in the mountainous basin analyzed herein. However, in the wavelet-based methodology we employ the Laplacian as initially proposed by *Lashermes et al.* [2007]. An exhaustive discussion of the advantages of one definition versus the other one can be found in work by *Passalacqua et al.* [2010].

[25] For extracting the channel network, *Passalacqua et al.* [2010] proposed the use of geodesic curves instead of the semiautomatic procedure developed by *Lashermes et al.* [2007]. A brief description of this technique follows (more details can be found in work by *Passalacqua et al.* [2010]). Geodesics are defined as curves of minimal cost among all the possible curves that connect two points a and b:

$$g(a,b) := \arg\left(\min_{C\in\Omega} \int_a^b \psi(s)ds\right) \quad (21)$$

where the function $\psi(C) : \Omega \rightarrow \mathbb{R}^+$ gives the cost of traveling on a curve $C \in \Omega$. The definition of the function ψ includes topographic attributes of the geomorphic feature we want to extract. In the case of channel extraction presented by *Passalacqua et al.* [2010], the cost function ψ includes surface curvature and flow accumulation, such that curves with positive curvature above threshold (defined from the quantile-quantile plot) and large flow accumulation are preferred to all the possible curves connecting two points. Note that, having defined the skeleton of likely channelized pixels through the curvature and slope direction change thresholds, geodesic curves are the curves of minimal cost ψ among the ones that connect two points (outlet and channel head) within the skeleton. Basically, the identification of the skeleton restricts the domain of existence of channels (where one or both the threshold criteria are not satisfied, we are sure that channels do not exist, and thus we do not include those areas in the search of geodesic curves). The main advantage of the geodesic optimization is the use of local information (slopes, curvatures, etc.) but in a global setting so that small errors and local discontinuities do not interrupt the algorithm of channel extraction, resulting in a fully automatic procedure. Note also that the algorithm automatically identifies channel heads as the points at which the skeleton stops. Because the skeleton is usually wider than one pixel, the point identified as a channel head is the point located at the end of the skeleton and at minimum geodesic distance from the outlet. Again, we refer the reader to *Passalacqua et al.* [2010] for an exhaustive discussion on the automatic selection of channel heads.

4. Comparison of the Extracted Channel Networks to Classical Methodologies

[26] Our goal in this section is to show the channel networks obtained by applying the wavelet-based extraction methodology [*Lashermes et al.*, 2007] and GeoNet [*Passalacqua et al.*, 2010] and to compare them to the surveyed channel

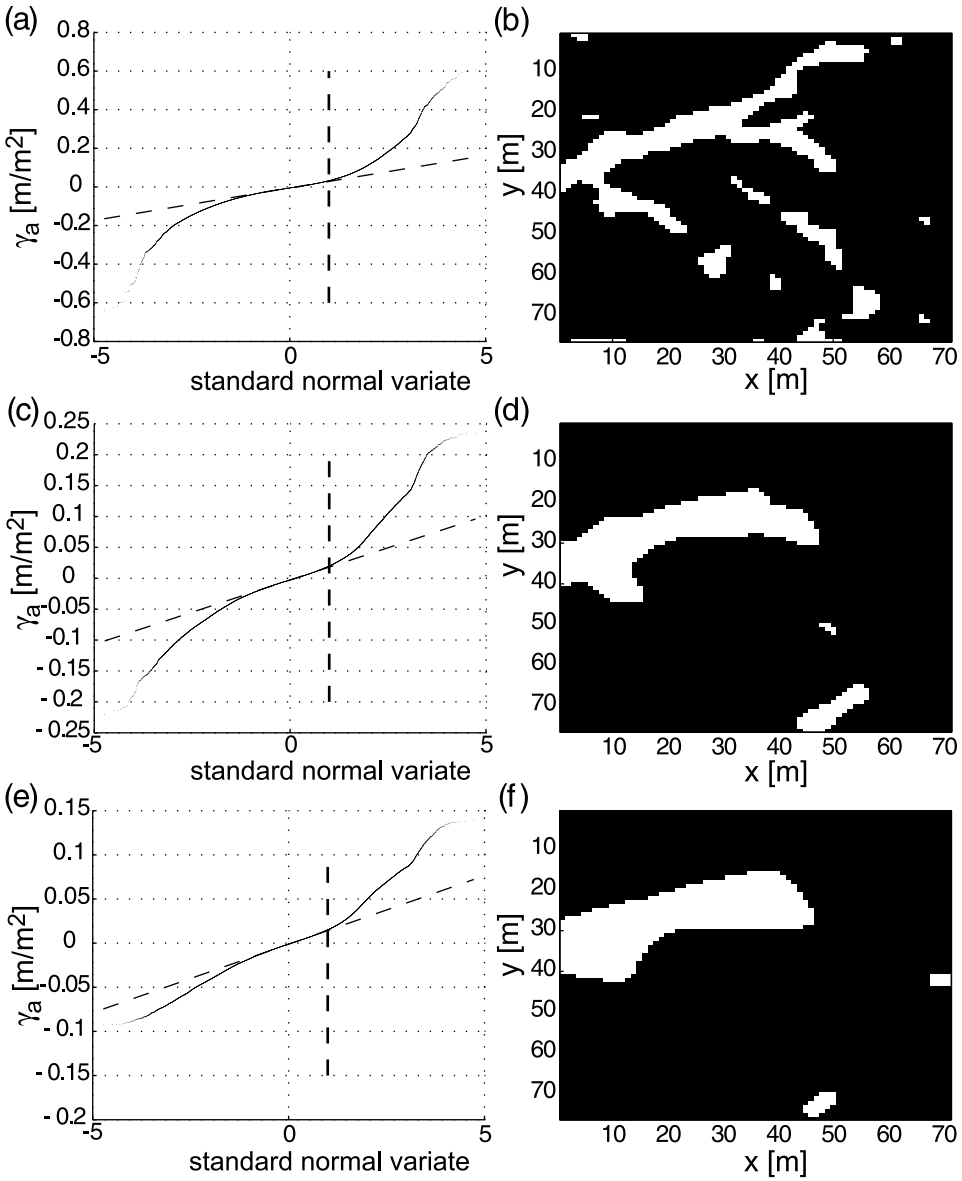

Figure 5. Quantile-quantile plot and corresponding skeleton for the Laplacian curvature computed with (a, b) σ = 2 m (a = 8.9 m), (c, d) σ = 4 m (a = 17.8 m), and (e, f) σ = 6 m (a = 26.7 m).

network shown in Figure 1. We also applied to the same data set two classical extraction methodologies based on an area threshold and a combination of area and slope threshold, with the area computed using the flow direction algorithm D8 [*O'Callaghan and Mark*, 1984], to assess the performance of the new generation of extraction methodologies versus the methodologies commonly in use.

4.1. Definition of the Scale of Analysis

[27] First, we need to define the scale (standard deviation of the Gaussian kernel and number of iterations for the geometric nonlinear methodology) employed in the two methodologies. As reported by *Passalacqua et al.* [2010], there is no direct relationship between the standard deviation of the kernel employed in the wavelet-based methodology, and the number of iterations of the nonlinear filtering operation employed in GeoNet. However, *Passalacqua et al.* [2010] showed the advantages of nonlinear versus linear filtering through a comparison of the two methodologies performed with t = 50 in both, assuming $t = \sigma^2$ in the wavelet-based methodology. Our interest in this paper is not in repeating this comparison, but in analyzing the capabilities of the two methodologies at their best performance for the analysis and the data employed here. Considering the resolution of the data of 1 m, we decided to use $\sigma = 1m$ as the minimum standard deviation of the Gaussian kernel. We recall here that the standard deviation of the kernel translates into different scales a in the elevation ($g_{0,\sigma,x,y}$ in (6), $a = 4\sigma$), in the gradient ($g_{1,\sigma,x,y}$ in (4), a given by (7)), and in the curvature ($g_{2,\sigma,x,y}$ in (5), a given by (8)). In order to work with approximately the same scale a in the gradient and curvature computation, we selected as minimum scales $\sigma = 1m$ for the gradient, and $\sigma = 2m$ for the curvature, which correspond approximately to a value of a around 7 m. The other scales here analyzed, for the wavelet based methodology, are

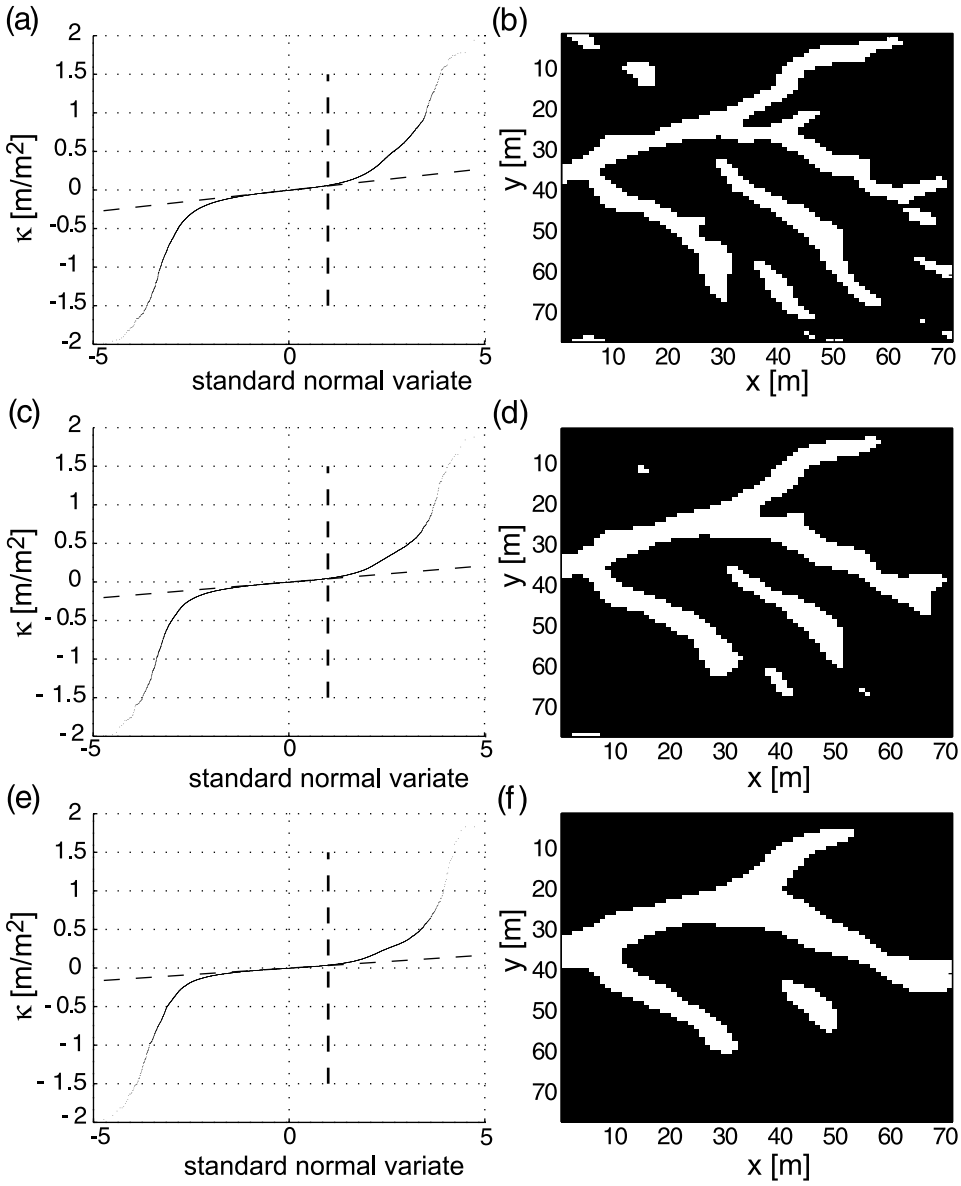

Figure 6. Quantile-quantile plot and corresponding skeleton for the geometric curvature computed after Perona-Malik filtering with (a, b) $t = 20$, (c, d) $t = 50$, and (e, f) $t = 100$.

$a = 17.8m$ (corresponding to $\sigma = 4m$ for curvature) and $a = 26.7m$ (corresponding to $\sigma = 6m$ for curvature). For the geometric nonlinear methodology, GeoNet, we selected as minimum scale that corresponding to $t = 20$ iterations, and $t = 50$ and $t = 100$ iterations as coarser scales. These values were selected following the approach used by *Passalacqua et al.* [2010] to achieve a similar level of overall smoothing in the linear and nonlinear filtering operations.

[28] We proceed now with assessing the optimal scale of analysis (not too small to suffer from noise but not too large to risk smoothing out features of interest) for the data at hand by plotting the skeleton of likely channelized pixels at different scales. For this part of the analysis we will simply refer to the skeleton based on curvature (without adding the slope direction change) as that will already give us an idea of the effect of scale on the results. In addition, we focus only on a small part of the basin, indicated as T1 in Figure 1, as it will be easier to assess differences among scales in a smaller part of the basin. Figure 5 shows the quantile-quantile plots of the Laplacian and the corresponding skeleton computed through the convolution with the wavelet $g_{2,\sigma,x,y}$ at scales $a = 8.9$ m (Figure 5a), $a = 17.8$ m (Figure 5b) and $a = 26.7$ m (Figure 5c). As it can be seen, the channels of the Rio Col Duro basin are very small and the corresponding channel heads very close to each other. At scale $a = 17.8$ m (Figure 5b) we can see how most of the channels are already not mapped. For this reason, we fixed the scale of analysis for the wavelet based methodology at the minimum ($\sigma = 1$ m for gradient and $\sigma = 2$ m for curvature). Figure 6 shows the quantile-quantile plots of the geometric curvature and the corresponding skeleton computed through finite differences after performing the Perona-Malik filtering with $t = 20$ (Figure 5a), $t = 50$ (Figure 5b) and $t = 100$ (Figure 5c) iterations. As in the case of the wavelet computation, although the skeletons appear in this case better defined, we fixed the scale of analysis at $t = 20$,

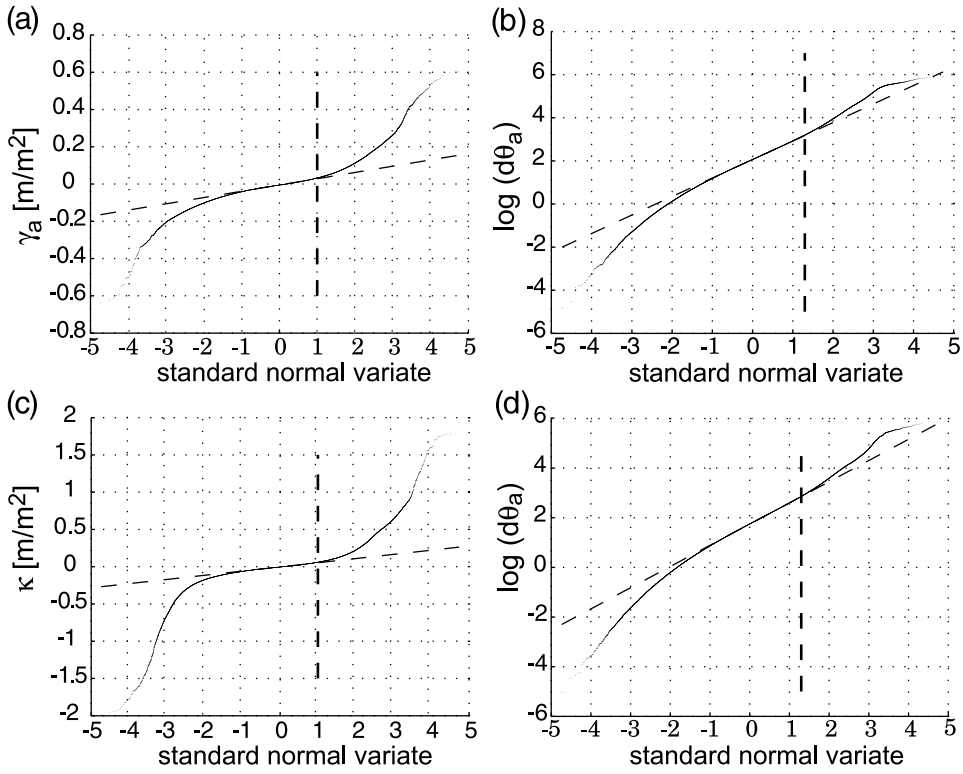

Figure 7. Quantile-quantile plots. (a) Laplacian computed with the Mexican hat wavelet with σ = 2 m (a = 8.9 m), (b) slope direction change computed with the first derivative of the Gaussian with σ = 1 m (a = 6.28 m), (c) geometric curvature computed through finite differences on the Perona-Malik filtered data (t = 20), and (d) slope direction change computed through finite differences on the Perona-Malik filtered data (t = 20). The deviations from the normal behavior indicate a transition in the statistical behavior of the system. These transitions correspond to a value of the standard normal deviate z = 1 for the quantile-quantile plots of curvature and to z = 1.3 for the quantile-quantile plots of slope direction change.

as already at t = 20 some of the smallest bifurcations and corresponding channel heads are not well detectable. An attempt to use $t \ll 20$ extracted too many isolated areas.

[29] Having defined the scales of analysis for the wavelet-based methodology and for GeoNet, we can now proceed with plotting the quantile-quantile plots and skeletons for the whole basin and extracting the channel networks.

4.2. Channel Network Extraction

[30] The large variability shown by channel initiation contributing areas mentioned in section 2 and shown in Figure 2, presents a formidable challenge for any standard channel network extraction algorithm. In the case of the geometric methodology proposed by *Passalacqua et al.* [2010] a small threshold in contributing area is used to achieve further narrowing of the skeleton of likely channelized pixels, an operation useful in improving the robustness of the minimum geodesic search of channels. In this case, a very small threshold of 100 m^2 was able to eliminate some pixels of the skeleton width without interfering with the channel heads. Note that, as pointed out by *Passalacqua et al.* [2010], the contributing area threshold is an arbitrarily chosen value, which might depend on the landscape in analysis. The only constrain in selecting this value is that it should be smaller than the smallest channel initiation area in that landscape, which in our case was 110 m^2.

[31] Figures 7a and 7b show the quantile-quantile plots of curvature (Laplacian) and slope direction change, computed using as wavelets the first and second derivatives of the Gaussian kernel with appropriate variance such that the scale is approximately a = 4 m, while Figures 7c and 7d show the corresponding plots for the geometric curvature and slope direction change computed through finite differences after performing 20 iterations (in time) of the Perona-Malik filter. It can be noticed by comparing Figure 7a with Figure 7c and Figure 7b with Figure 7d that the value of the standard normal variate z at which the deviation from normal and lognormal behaviors are observed (namely z = 1 for curvature and z = 1.3 for slope direction change), are methodology-independent, as expected since this value is representative of the statistical intrinsic behavior of the system, rather then the particular processing or the computational methodology employed.

[32] After having identified the thresholds for the curvature and slope direction change, we can extract the skeleton of the likely channelized pixels, as described in section 3. Figure 8a shows the skeleton obtained through the wavelet-based methodology, while Figure 8b shows the skeleton obtained through the nonlinear geometric methodology. At the scale of the whole basin it is difficult to capture the

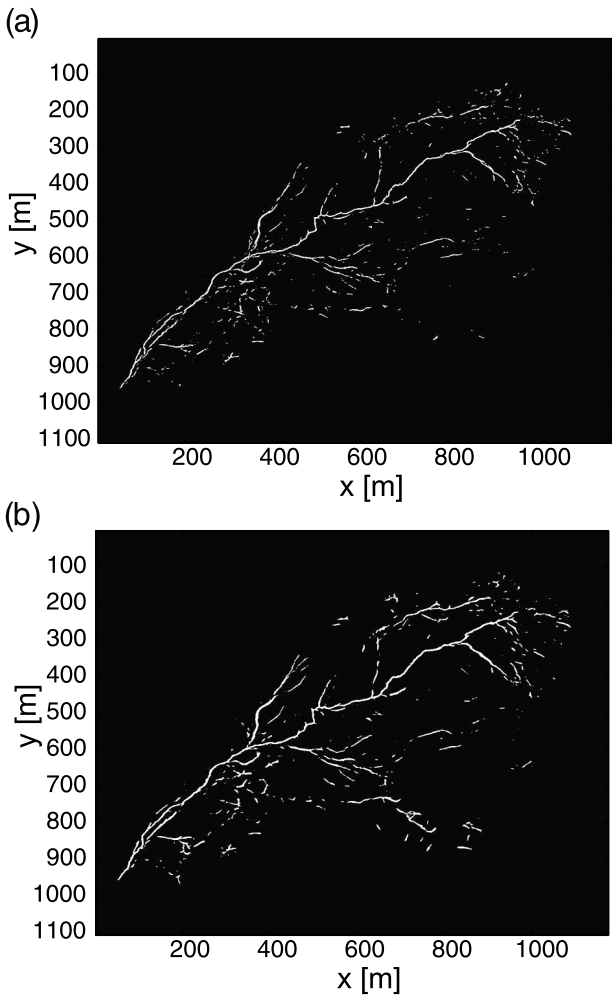

Figure 8. (a) Skeleton obtained by thresholding curvature and slope direction change computed through wavelets at approximately $a = 7$ m. (b) Skeleton obtained by thresholding geometric curvature and slope direction change computed through finite differences on the Perona-Malik filtered data after $t = 20$.

differences among the two skeletons. However, the differences are succinctly highlighted in section 5, which focuses on channel head detection. For now, we want to point out that these are the two skeletons used in the sequel for extracting the channel networks shown in Figures 9a and 9b. Figure 9 shows the comparison of the channel network extracted (plotted in yellow) using the wavelet-based methodology (Figure 9a); the geometric nonlinear methodology (Figure 9b); an area threshold $A_1 = 3099$ m^2 (Figure 9c); a combination of area and slope $AS^y > T_1$ with $y = 2$ [*Montgomery and Dietrich*, 1992] and $T_1 = 221$ m^2 (Figure 9d) to the surveyed channels (plotted in red). The values of A_1 and T_1 are given by the mean of the drainage areas [*O'Callaghan and Mark*, 1984] and the product of mean area and mean slope squared, respectively, both measured at the 16 surveyed channel heads. We can notice how the classical methodologies tend to predict channels that are actually not present in the field. This is the case, in particular, in one side of the basin (see arrows in Figures 9c and 9d). This area is characterized by large and unchannelized hillslopes. Classical methodologies identify here several channels due to the large drainage area, which, however, are not present in the field. The wavelet-based methodology and the geometric nonlinear methodology show more realistic extracted channel networks. The channel in the lower side of the basin detected by the geometric nonlinear methodology corresponds to an ancient channel, mapped on historical maps, but not surveyed (see channel marked by B in Figure 9b).

[33] It has to be noted here that the wavelet-based extraction is partially subjective, as the user decides which channels to trace, based on the continuity of the skeleton. Because the skeleton in this area was very discontinuous, as can be seen from the skeleton in Figure 8, we decided not to trace it with the wavelet-based methodology.

5. Channel Head Detection

[34] In this section we focus on the capability of the wavelet-based methodology and of GeoNet in detecting channel head locations. First, we will use the channel networks extracted in section 4, to measure the performance of the two methodologies on the whole basin. Then, we will focus on three small areas of different morphological characteristics to study the dependence of the performance on the landscape type. Figure 10 shows the histogram of the distances between the surveyed channel heads and the detected channel initiation locations on the skeleton (at the end of the extracted channel) obtained with the wavelet-based methodology (Figure 10a) and GeoNet (Figure 10b). We measured these distances on the whole basin in correspondence with the 16 surveyed channel heads. In the case in which the skeleton did not detect the channel head, that particular location was excluded. This happened in particular in the area T2 (see Figure 1), where, as explained later, the channel detection is particularly challenging because of the local geomorphological characteristics of the basin. We obtained 12 measured distances for the wavelet-based methodology and 13 for GeoNet, out of a total of 16 field-mapped channel heads. As can be seen from Figure 10, the distances between the surveyed and the detected channel initiation is less than 5 m for most of the channels, meaning that our thresholding criteria are geomorphologically appropriate for the basin of study. Only for one channel head, indicated as c_1 in Figure 1, both methodologies detected channel initiation far from the actual location of the channel head (see the largest values in Figures 10a and 10b). This is due to the fact that the skeletons detect a convergent area upstream of the location of c_1 which is in fact present in the field, but without any incision or erosion.

[35] Now we focus on three small areas (T1, T2, and T3) indicated by the boxes in Figure 1. The aim of this part of the analysis is to test the two methodologies described above, in terms of their capability of detecting channel heads in areas with different morphology. The area T2 is characterized by gentle slopes (mean slope value of 16°), the area T3 by steep slopes (mean slope value of 30°) and the presence of a narrow valley. The area T1 has characteristics in between of the two.

5.1. Test Area T1

[36] Figure 11a shows the skeleton of likely channelized pixels in test area T1, obtained through thresholding curva-

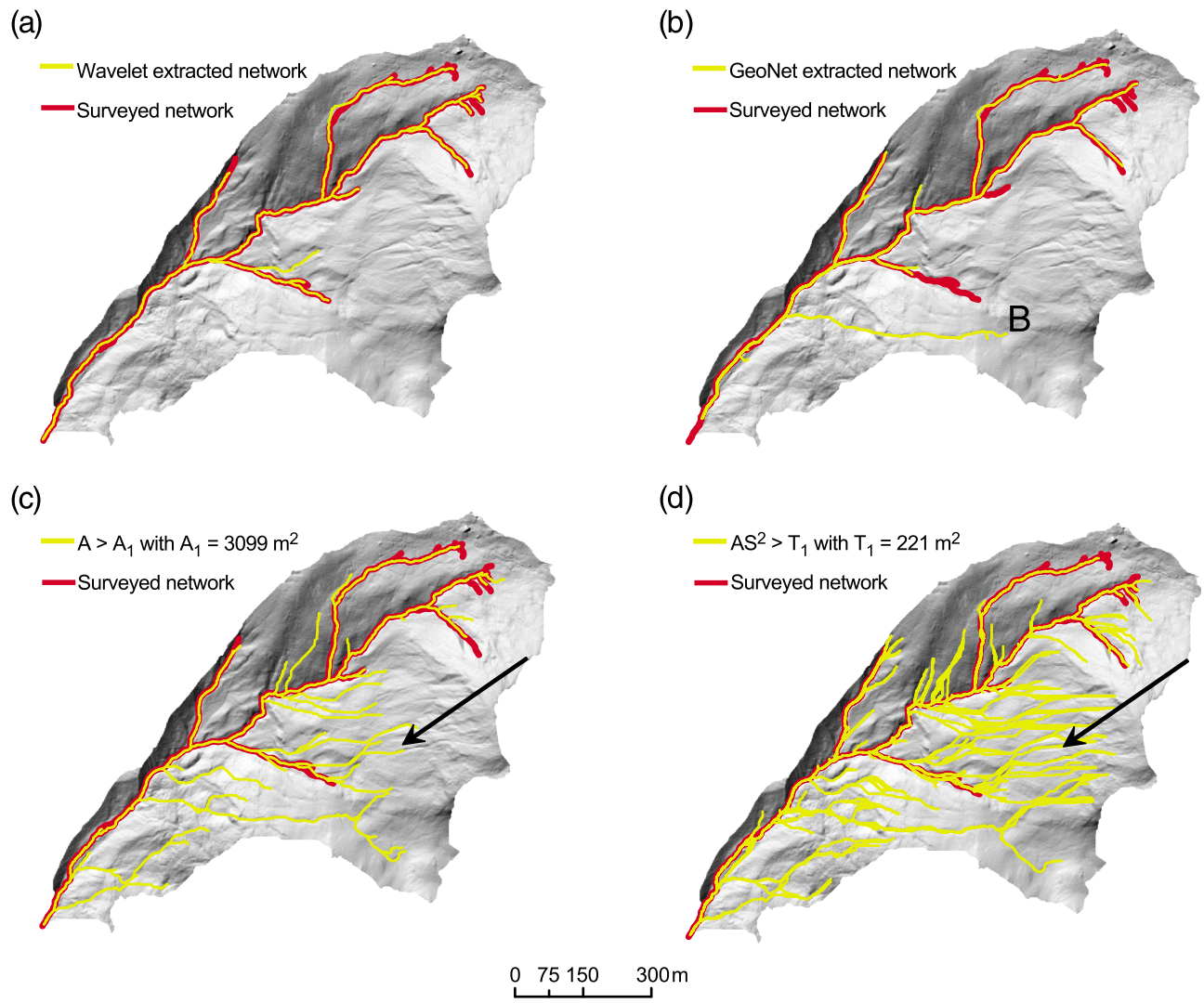

Figure 9. Channel networks extracted using different methodologies and compared to the surveyed one. (a) The wavelet-based methodology, (b) GeoNet, (c) an area threshold A_1 = 3099 m^2, and (d) a combination of area and slope $AS^y > T_1$ with y = 2 and T_1 = 221 m^2. The letter B in (Figure 9b) indicates an ancient channel mapped by GeoNet and reported in historical maps of the area but not surveyed. The arrows in Figures 9c and 9d indicate the side of the basin where the two classical methodologies tend to predict channels which are not present in the field.

ture and slope direction change computed through wavelets, as prescribed by the *Lashermes et al.* [2007] methodology, at a scale of approximately a = 7 m (see Figure 7). We can compare Figure 11a with Figure 11b, obtained through nonlinear filtering after t = 20 iterations and thresholding curvature and slope direction change (see Figure 7). We notice that both the skeletons identify appropriately channel initiation, but the skeleton obtained through nonlinear filtering, Figure 11b, shows less disrupted channels. In an area where no significative landslides are present, such as this one, as it can be seen from Figure 1, channels are expected to be continuous.

[37] While the wavelet methodology proposed by *Lashermes et al.* [2007] does not perform an automatic detection of the channel heads, as the channels are traced in a semiautomatic fashion from the outlet to the sources, thus stopping at user's discretion, the geometric nonlinear methodology proposed by *Passalacqua et al.* [2010] automatically detects channel heads, as mentioned in section 3 and fully described by *Passalacqua et al.* [2010]. As previously discussed, before automatically detecting channel heads, noise is further reduced by introducing an additional threshold in the drainage area, here chosen equal to 100 m^2. This operation allows to obtain a narrower and more defined skeleton, as shown in Figure 11c, where the automatically detected channel heads are compared to the surveyed ones. The extracted channel heads are located approximately 3 m, 5 m, 8 m, and 2 m (top to bottom) from their surveyed locations.

5.2. Test Areas T2 and T3

[38] Figures 12a and 12b show the skeletons of likely channelized pixels obtained through thresholding curvature and slope direction change computed for the test area T2

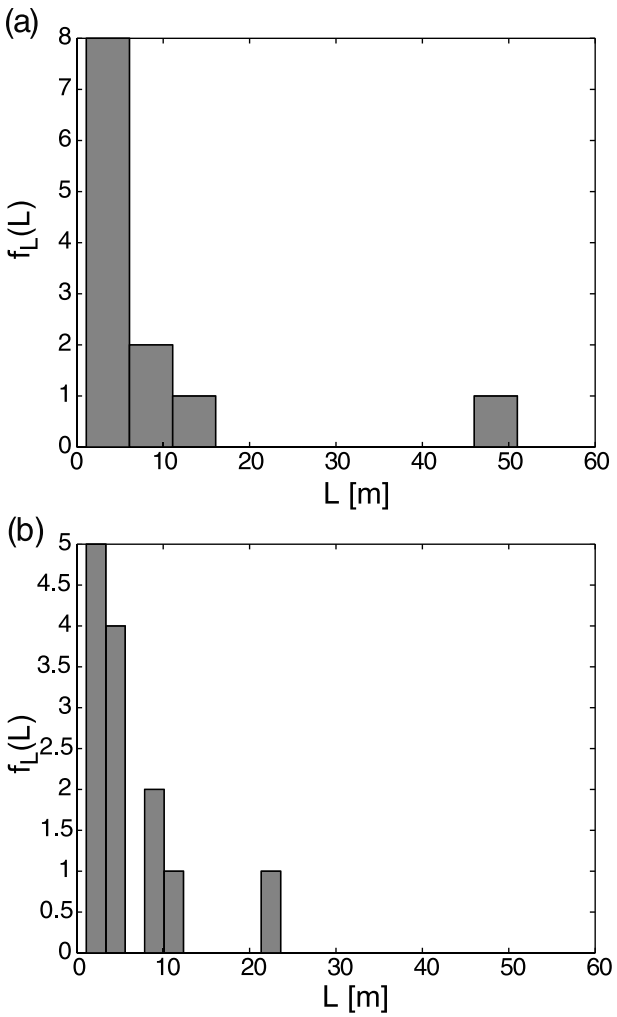

Figure 10. Histogram of the distances between surveyed channel heads and detected channel initiation points within the skeleton from (a) the wavelet-based methodology and (b) the geometric nonlinear methodology.

through wavelets at scale a = 7 m (Figure 12a), and computed through finite differences on the Perona-Malik filtered data after t = 20 iterations (Figure 12b). Looking at Figures 12a and 12b one can observe that the channel recognition carried out with the finite differences on the Perona-Malik filtered data reduces the inclusion of isolated small convergent areas as part of the skeleton of likely channelized pixels. Thus, the geometric approach allows for a more robust detection of the channels compared to the wavelet-based methodology. The results obtained in the test area T3 (Figures 13a and 13b) show that the two methodologies perform equally well. In this case, where steep slopes prevail and the valley is deeply incised, both methodologies recognize in detail the convergent areas without capturing at the same time the small isolated convergent areas located nearby. The different performance of the two methodologies in two different morphological areas addresses an interesting finding: where low slopes prevail, the nonlinear filtering combined with finite difference computations employed in GeoNet results in more accurate

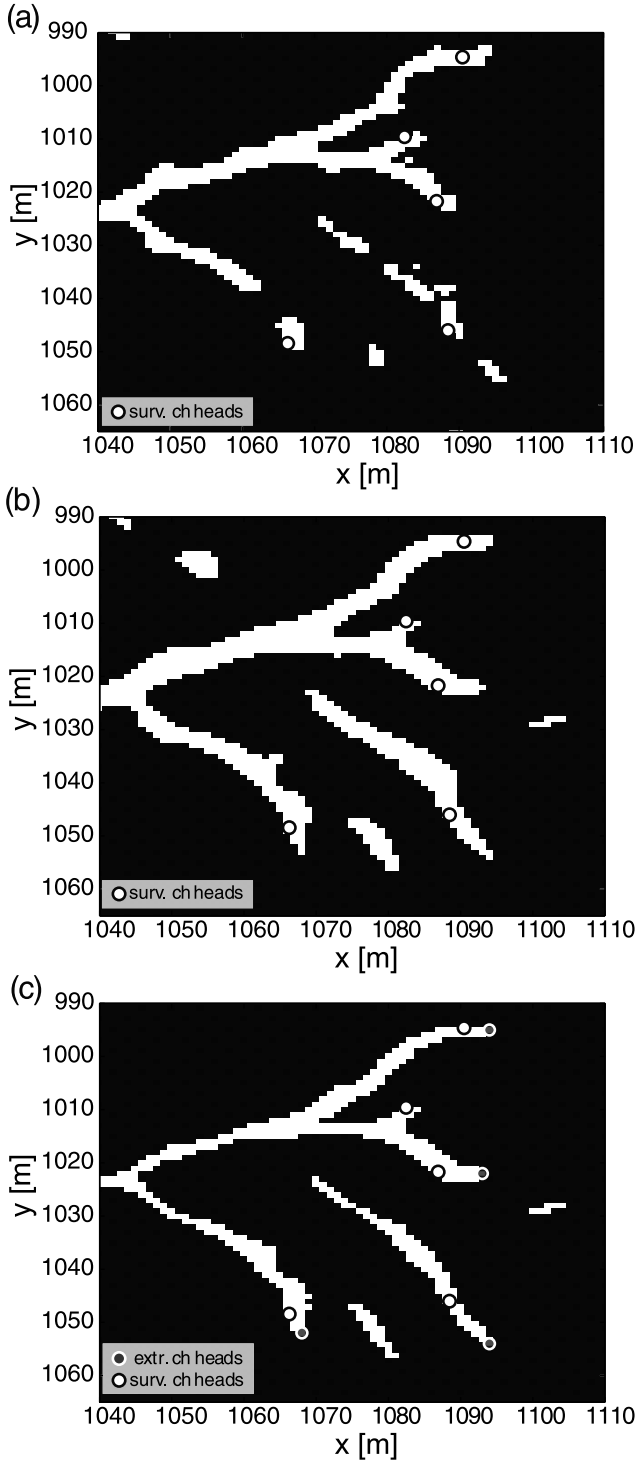

Figure 11. Test area T1: (a) skeleton obtained by thresholding curvature and slope direction change computed through wavelets at approximately $a = 7$ m and (b) skeleton obtained by thresholding geometric curvature and slope direction change computed through finite differences on the Perona-Malik filtered data after $t = 20$. Skeleton obtained by thresholding geometric curvature and slope direction change computed through finite differences on the Perona-Malik filtered data after $t = 20$, in addition to a small threshold drainage area of 100 m^2. (c) Comparison between the extracted (shown as gray circles) and the surveyed channel heads (shown as white circles).

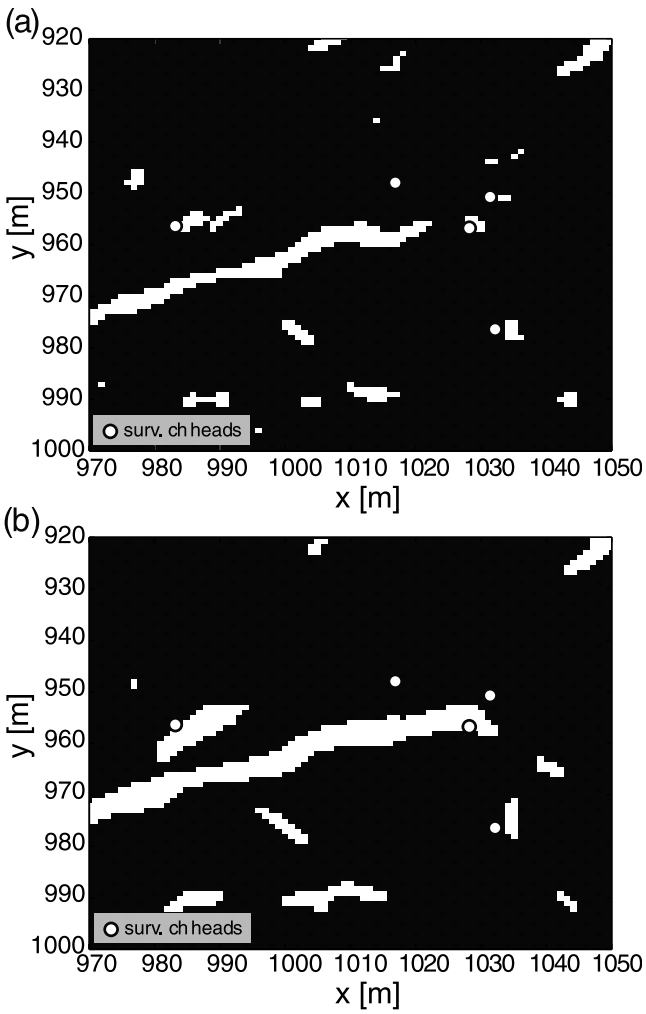

Figure 12. Test area T2: (a) skeleton obtained through thresholding curvature and slope direction change computed through wavelets at scale $a = 7$ m and (b) skeleton obtained through finite differences on the Perona-Malik filtered data after $t = 20$ iterations. In Figures 12a and 12b the surveyed channel heads are shown as white circles. This test area is characterized by low slopes. It can be seen that GeoNet results in a more accurate and robust extraction of channels heads compared to the wavelet-based methodology.

and robust extraction of channels compared to the wavelet-based methodology.

6. Channel Disruption Analysis

[39] We now test the ability of the two methodologies described above in detecting channel disruptions, which in this basin would be mostly attributed to landslides. We focus this analysis on the black dotted rectangle ("landslide test area" in Figure 1), located in the lower left part of the boundary (partly outside) of the Rio Col Duro basin. Figure 14a shows the skeleton obtained by thresholding curvature and slope direction change computed through wavelets, while Figure 14b shows the same skeleton obtained on the Perona-Malik filtered data and employing the geometric curvature. Figures 14a and 14b show also the location of several surveyed initiation areas of shallow landslides, here plotted in gray. Note the channel disruption correspondent to the largest landslide surveyed on the landscape (see A in Figure 14). Both skeletons were found interrupted at this location. In the other cases we can notice that the landslides are always located laterally with respect to the channel, and none of the channels overlaps an existing landslide. This shows that the thresholding criteria chosen serve the purpose of tracing the channels in their actual location, and identifying disruptions of interest. Also in this case, the results are interesting since a classical channel extraction methodology would have not been able to highlight the presence of these disruptions, as channels would be traced continuously throughout the basin with no possibility of detecting the presence of landslides and their possible consequences in channel form.

7. Effect of Linear Versus Nonlinear Filtering on Extracting Channel Cross Sections

[40] We analyze in this section the effect of Gaussian filtering versus nonlinear Perona-Malik filtering on extracting

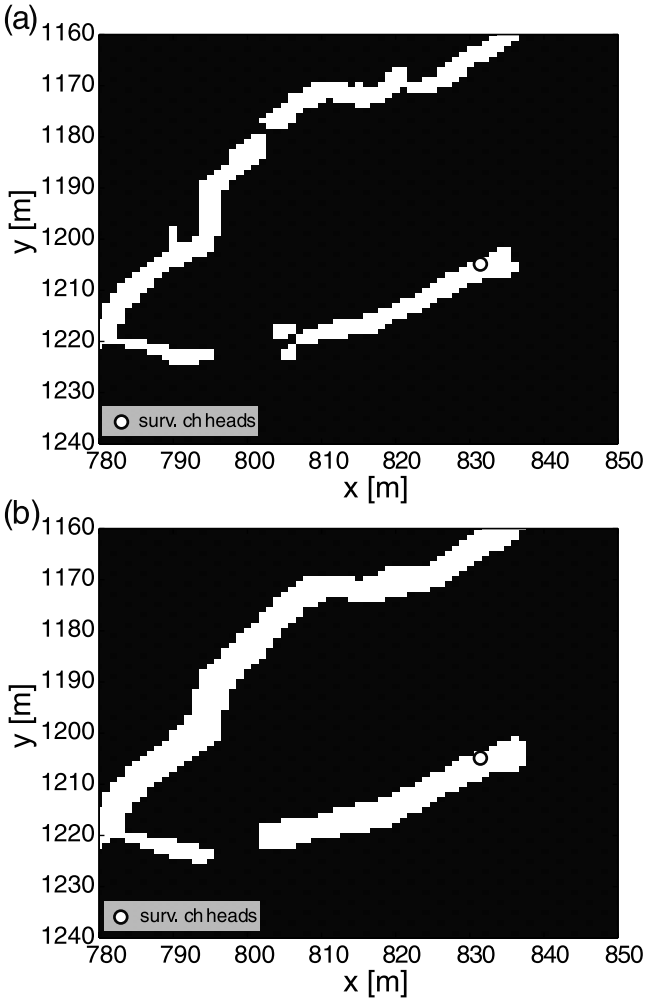

Figure 13. Test area T3: (a) skeleton obtained through thresholding curvature and slope direction change computed through wavelets at scale $a = 7$ m and (b) skeleton obtained through finite differences on the Perona-Malik filtered data after $t = 20$ iterations. In Figures 13a and 13b the surveyed channel heads are shown as white circles. This test area is characterized by steep slopes, and the two methodologies perform equally well.

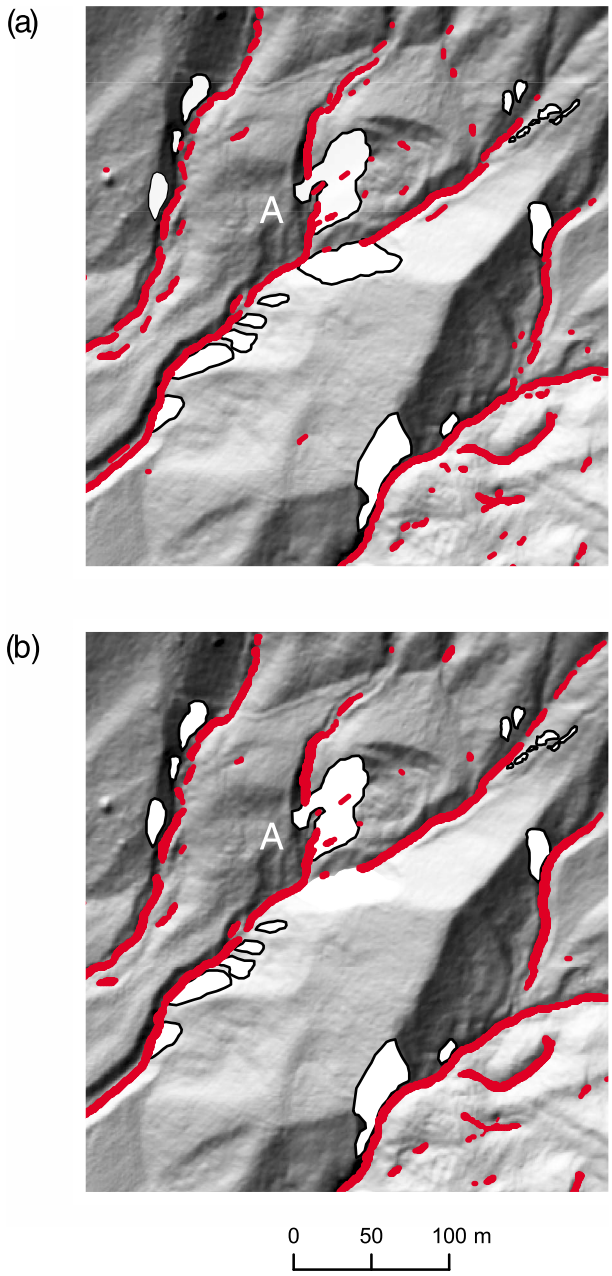

Figure 14. Skeleton obtained (a) by thresholding curvature and slope direction change computed through wavelets at approximately a = 7 m and (b) through finite differences on the Perona-Malik filtered data after t = 20 iterations. In Figures 14a and 14b the surveyed landslides are shown as white patches. Note that both skeletons are interrupted in correspondence to the largest landslide, indicated as A.

channel cross sections in the Rio Col Duro basin. In particular, as it can be seen in Figure 1, we extracted three cross sections, one in the colluvial channel within a gentle slope area (labeled as CS1 in Figure 1), one in the bedrock channel (labeled as CS2 in Figure 1) and the third one in the alluvial channel (labeled as CS3 in Figure 1). Figures 15a–15c show the original cross section and the ones cut after performing Gaussian or nonlinear filtering on the elevation data. In the case of Gaussian filtering we have used two smoothing scales, namely σ = 1 m, which corresponds to

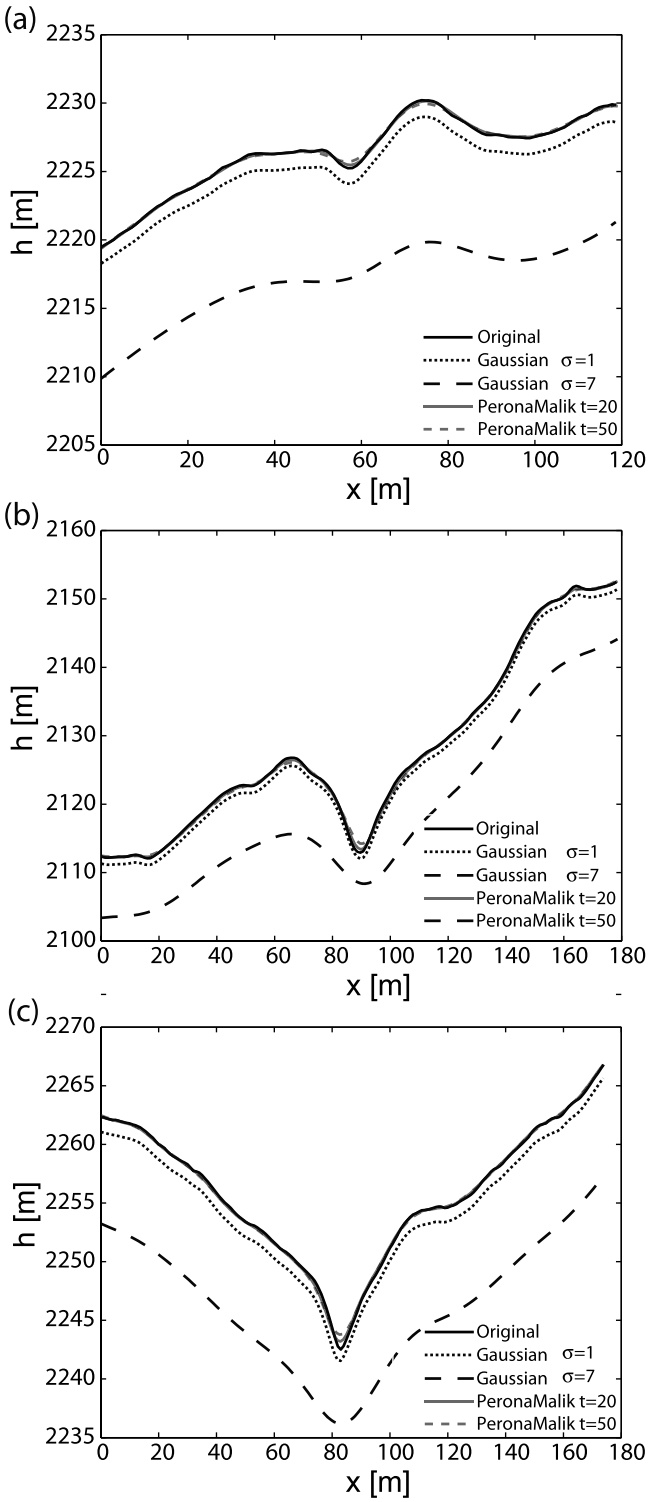

Figure 15. Cross sections cut along the Rio Col Duro main stem river: (a) colluvial channel CS1, (b) bedrock channel CS2, and (c) alluvial channel CS3. In all three cross sections, independently of the local geological characteristics, Gaussian filters of increasing scale tend to shift the centerline of the channel and lower the elevation of the landscape. Notice in particular Figure 15a where the left bank of the channel ends up disappearing.

$a \cong 4m$ ($a = 4\sigma$ for elevation), and $\sigma = 7$ m, which corresponds to $a \cong 28m$. For the nonlinear filtering, we have performed 20 and 50 iterations, respectively. In all the three cross sections, independently of the local geological characteristics, we can notice how Gaussian filters of increasing scale tend to shift more and more the centerline of the channel and also lower the elevation of the landscape. Furthermore, increasing the scale, the cross sections become increasingly smoothed, and in particular in the case of cross section 2 (colluvial channel, Figure 15a) the left bank of the channel ends up disappearing. This has an effect on the channel extraction itself, resulting in increasingly disrupted skeletons of likely channelized pixels, even in areas with no landslides present. Thus it is concluded that nonlinear filtering of landscapes offers advantages for both channel network extraction and for the extraction of channel cross sections.

[41] Looking at Figures 15a–15c it is also interesting to note how clear is the different morphology of the colluvial channel cross section compared to the bedrock and alluvial ones. Bedrock and alluvial channels are deeply incised and are located in the steep slope area of the Rio Col Duro basin, while the colluvial channel presents shallow incision and smoothed topography. This channel is located in the gentle slope area of the basin, where the employment of nonlinear filtering is recommended.

8. Conclusions

[42] This work presents a comparison of the capability of two geomorphic feature extraction methodologies in extracting the channel network, capturing channel heads, detecting relevant channel disruptions corresponding to landslides and extracting representative channel cross sections in a complex mountainous landscape, where both gentle and steep slope areas are present. The analysis has been carried out in a small headwater alpine basin, where several field surveys were conducted during the past few years, such as channel network and channel head survey, landslide scars mapping, and lidar survey. All the analyses presented in this work are based on a 1 m lidar derived DTM.

[43] In general, the two methodologies, purely based on the detection of local morphology by the use of local slope and landform curvature, present significant advantages with respect to the traditional methodologies for channel network extraction based on drainage area and local slope thresholds. Our study area exhibits a large variability in the values of drainage area at the channel heads and thus it would be impossible to capture such variability with a unique threshold value for drainage area, as would be required by a classical extraction methodology.

[44] In detail the results suggest the following.

[45] 1. Local nonlinear filtering combined with the global geodesic optimization used in GeoNet [*Passalacqua et al.*, 2010] is more computationally robust, achieving better localization and extraction of features, compared to the wavelet-based methodology [*Lashermes et al.*, 2007].

[46] 2. Where steep slopes prevail and the valley is deeply incised, both methodologies recognize in detail the convergent areas.

[47] 3. Where low slopes prevail, nonlinear filtering and finite difference computations as employed in GeoNet should be considered optimal.

[48] 4. Both methodologies capture channel disruptions due to landslide activity, even though the wavelet-based skeleton appears more noisy and discontinuous. Also in this case a classical channel extraction methodology would have not been able to highlight the presence of these disruptions, as channels would be traced continuously throughout the basin.

[49] 5. Looking at the extracted cross sections, Gaussian filtering of increasing scale tends to shift more and more the centerline of the channel, while nonlinear filtering achieves better channel centerline localization and shows little deformation of the landscape contours.

[50] The availability of high-resolution topography combined with these two morphometric methodologies represents a powerful new approach for advancing automatic feature extraction and thus advance the study of earth surface processes in terms of better understanding of process from form, development of landscape evolution models, and parameterization of relevant landscape features into geomorphic transport and hydrologic models.

[51] **Acknowledgments.** This work has been supported by the National Center for Earth-surface Dynamics (NCED), a Science and Technology Center funded by NSF under agreement EAR-0120914. The lidar surveys were partly founded by the Italian Ministry of University and Research GRANT PRIN 2005 "National network of experimental basins for monitoring, and modeling of hydrogeological hazard." The airborne lidar data were elaborated by the Interdepartmental Research Center for Cartography, Photogrammetry, Remote Sensing and GIS at the University of Padova (CIRGEO). Computer resources were provided by the Minnesota Supercomputing Institute, Digital Technology Center at the University of Minnesota. We thank the Editor, Associate Editor, and three anonymous reviewers for insightful comments which improved our work.

References

Ackerman, F. (1999), Airborne laser scanning—Present status and future expectations, *ISPRN J. Photogramm. Remote Sens.*, *54*, 64–67.

Ardizzone, F., M. Cardinali, M. Galli, F. Guzzetti, and P. Reichenbach (2007), Identification and mapping of recent rainfall-induced landslides using elevation data collected by airborne LiDAR, *Nat. Hazards Earth Syst. Sci.*, *7*, 637–650.

Band, L. E. (1986), Topographic partition of watersheds with digital elevation models, *Water Resour. Res.*, *22*, 15–24.

Briese, C. (2004), Breakline modeling from airborne laser scanner data, Ph.D. thesis, Inst. of Photogramm. and Remote Sens., Vienna Univ. of Technol., Vienna.

Cavalli, M., and L. Marchi (2007), Characterization of the surface morphology of an alpine alluvial fan using airborne LiDAR, *Nat. Hazards Earth Syst. Sci.*, *8*, 323–333.

Cavalli, M., P. Tarolli, L. Marchi, and G. Dalla Fontana (2008), The effectiveness of airborne LiDAR data in the recognition of channel bed morphology, *Catena*, *73*, 249–260, doi:10.1016/j.catena.2007.11.001.

Dalla Fontana, G., and L. Marchi (2003), Slope-area relationships and sediment dynamics in two alpine streams, *Hydrol. Processes*, *17*, 73–87.

Dietrich, W. E., and T. Dunne (1993), The channel head, in *Channel Network Hydrology*, edited by K. Bevan and M. J. Kirkby, pp. 175–219, John Wiley, Chichester, U. K.

Dietrich, W. E., C. J. Wilson, D. R. Montgomery, and J. McKean (1993), Analysis of erosion thresholds, channel networks and landscape morphology using a digital terrain model, *J. Geol.*, *3*, 161–180.

Frankel, K. L., and J. F. Dolan (2007), Characterizing arid region alluvial fan surface roughness with airborne laser swath mapping digital topographic data, *J. Geophys. Res.*, *112*, F02025, doi:10.1029/2006JF000644.

Glenn, N. F., D. R. Streutker, D. J. Chadwick, G. D. Tahckray, and S. J. Dorsch (2006), Analysis of LiDAR-derived topography information for characterizing and differentiating landslide morphology and activity, *Geomorphology*, *73*, 131–148.

Heine, R. A., C. L. Lant, and R. R. Sengupta (2004), Development and comparison of approaches for automated mapping of stream channel networks, *Ann. Assoc. Am. Geogr.*, *94*(3), 477–490.

Kraus, K., and N. Pfeifer (2001), Advanced DTM generation from LiDAR data, *Int. Arch. Photogramm. Remote Sens.*, *34*, 23–35.

Kumar, P., and E. Foufoula-Georgiou (1997), Wavelet analysis for geophysical applications, *Rev. Geophys.*, *35*(4), 385–412.

Lashermes, B., E. Foufoula-Georgiou, and W. E. Dietrich (2007), Channel network extraction from high resolution topography using wavelets, *Geophys. Res. Lett.*, *34*, L23S04, doi:10.1029/2007GL031140.

Lenzi, M. A. (2001), Step-pool evolution in the Rio Cordon, northeastern Italy, *Earth Surf. Processes Landforms*, *26*, 991–1008.

Lenzi, M. A., L. Mao, and F. Comiti (2003), Interannual variation of suspended sediment load and sediment yield in an Alpine catchment, *Hydrol. Sci. J.*, *48*(6), 899–915.

Lenzi, M. A., L. Mao, and F. Comiti (2004), Magnitude-frequency analysis of bed load data in Alpine boulder bed stream, *Water Resour. Res.*, *40*, W07201, doi:10.1029/2003WR002961.

Mallat, S. (1998), *A Wavelet Tour of Signal Processing*, Academic, San Diego, Calif.

Mark, D. M. (1988), Network models in geomorphology, in *Modeling Geomorphological Systems*, edited by M. G. Anderson, pp. 73–97, John Wiley, New York.

McKean, J., and J. J. Roering (2004), Objective landslide detection and surface morphology mapping using high-resolution airborne laser altimetry, *Geomorphology*, *57*, 331–351, doi:10.1016/S0169-555X(03)00164-8.

Montgomery, D. R., and J. M. Buffington (1997), Channel-reach morphology in mountain drainage basins, *Geol. Soc. Am. Bull.*, *109*(5), 596–611.

Montgomery, D. R., and W. E. Dietrich (1989), Channel initiation, drainage density and slope, *Water Resour. Res.*, *25*, 1907–1918.

Montgomery, D. R., and W. E. Dietrich (1992), Channel initiation and the problem of landscape scale, *Science*, *255*, 826–830.

O'Callaghan, J., and D. Mark (1984), The extraction of drainage networks from digital elevation models, *Comput. Visualization Graph. Image Process.*, *28*, 328–344.

Passalacqua, P., T. Do Trung, E. Foufoula-Georgiou, G. Sapiro, and W. E. Dietrich (2010), A geometric framework for channel network extraction from LiDAR: Nonlinear diffusion and geodesic paths, *J. Geophys. Res.*, *115*, F01002, doi:10.1029/2009JF001254.

Perona, P., and J. Malik (1990), Scale-space and edge detection using anisotropic diffusion, *IEEE Trans. Pattern Anal. Machine Intell.*, *12*, 629–639.

Pirotti, F., and P. Tarolli (2010), Suitability of LiDAR point density and derived landform curvature maps for channel network extraction, *Hydrol. Processes*, *24*, 1187–1197, doi:10.1002/hyp.7582.

Rodriguez-Iturbe, I., and A. Rinaldo (1997), *Fractal River Basins. Chance and Self-Organization*, 528 pp., Cambridge Univ. Press, New York.

Slatton, K. C., W. E. Carter, R. L. Shrestha, and W. E. Dietrich (2007), Airborne laser swath mapping: Achieving the resolution and accuracy required for geosurficial research, *Geophys. Res. Lett.*, *34*, L23S10, doi:10.1029/2007GL031939.

Smith, M. J., J. Rose, and S. Booth (2006), Geomorphological mapping of glacial landforms from remotely sensed data: An evaluation of the principal data sources and an assessment of their quality, *Geomorphology*, *76*, 148–165, doi:10.1016/j.geomorph.2005.11.001.

Staley, D. M., T. A. Wasklewicz, and J. S. Blaszczynski (2006), Surficial patterns of debris flow deposition on alluvial fans in Death Valley, CA using airborne laser swath mapping, *Geomorphology*, *74*, 152–163.

Tarboton, D. G., R. L. Bras, and I. Rodriguez-Iturbe (1989), The analysis of river basins and channel networks using digital terrain data, *Rep. 326*, Ralph M. Parson Lab., Dep. of Civ. Eng., Mass. Inst. of Technol, Cambridge.

Tarboton, D. G., R. L. Bras, and I. Rodriguez-Iturbe (1991), On the extraction of channel networks from digital elevation data, *Hydrol. Processes*, *5*, 81–100.

Tarolli, P., and G. Dalla Fontana (2009), Hillslope to valley transition morphology: New opportunities from high resolution DTMs, *Geomorphology*, *113*, 47–56, doi:10.1016/j.geomorph.2009.02.006.

Tarolli, P., and D. G. Tarboton (2006), A new method for determination of most likely landslide initiation points and the evaluation of digital terrain model scale in terrain stability mapping, *Hydrol. Earth Syst. Sci.*, *10*, 663–677.

Tarolli, P., M. Borga, and G. Dalla Fontana (2008), Analyzing the influence of upslope bedrock outcrops on shallow landsliding, *Geomorphology*, *93*, 186–200.

Tarolli, P., J R. Arrowsmith, and E. R. Vivoni (2009), Understanding Earth surface processes from remotely sensed digital terrain models, *Geomorphology*, *113*, 1–3, doi:10.1016/j.geomorph.2009.07.005.

Trevisani, S., M. Cavalli, and L. Marchi (2010), Reading the bed morphology of a mountain stream: A geomorphometric study on high resolution topographic data, *Hydrol. Earth Syst. Sci.*, *14*, 393–405.

Vianello, A., and V. D'Agostino (2007), Bankfull width and morphological units in an alpine stream of the Dolomites (northern Italy), *Geomorphology*, *83*, 266–281, doi:10.1016/j.geomorph.2006.02.023.

Vianello, A., M. Cavalli, and P. Tarolli (2009), LiDAR-derived slopes for headwater channel network analysis, *Catena*, *76*, 97–106, doi:10.1016/j.catena.2008.09.012.

E. Foufoula-Georgiou and P. Passalacqua, National Center for Earth-Surface Dynamics, Department of Civil Engineering, University of Minnesota-Twin Cities, 23rd Ave. SE, Minneapolis, MN 55414, USA. (efi@umn.edu)

P. Tarolli, Department of Land and Agroforest Environments, University of Padova, Agripolis, Viale dell'Università 16, Legnaro, Padova I-35020, Italy.